Journal of Materials Chemistry B

ROYAL SOCIETY OF CHEMISTRY

PAPER

View Article Online
View Journal

Cite this: DOI: 10.1039/d6tb00577b

Ligand-mediated formation of amphiphilic silver nanoclusters: synthesis, redox properties, and activity against clinically relevant bacteria

Alexandru-Milentie Hada, [a] Marco Abbate,[b] Markus Zetes,[a] Ana Laura Coria-Gutiérrez, [b] Ana-Maria Craciun, [a] Nina Burduja,[bc] Chiara Abate, [b] Francisco J. Terán, [d] Milica Todea,[ae] Antonino Mazzaglia, [c] Angela Scala, [b] Antonia Nostro [b] and Anna Piperno *[b]

Ultrasmall silver nanoclusters have emerged as promising tools for their sensing, optical, and biological properties, but their translation toward practical applications remains limited due to the synthetic complexity and insufficient control over colloidal stability. Here we report a straightforward one-step strategy for the direct conversion of Ag^+ ions into blue-emitting silver nanoclusters (FcCAR@Ag NCs, average diameter 2.6 nm) using amphiphilic ferrocene carnosine (FcCAR) as both reducing and capping agents. Under mild basic conditions and in the presence of ascorbic acid, the FcCAR ligand drives the kinetic-controlled reduction of silver ions and simultaneously stabilizes the resulting nanoclusters through interfacial interactions mediated by ferrocene and carnosine functional groups. The formation of well-dispersed nanoclusters is confirmed by comprehensive optical, structural, and colloidal characterization, revealing blue photoluminescence and high colloidal stability. Cyclic voltammetry (CV) and differential pulse voltammetry (DPV) analyses performed on screen-printed electrodes (SPEs) showed a higher electrochemical response of FcCAR@Ag NCs with respect to the native FcCAR ligand, suggesting the potential application of FcCAR@Ag NCs in electrochemical sensing. Moreover, the use of ligands based on peptides functionalized with ferrocene units introducing lipophilicity confers an amphiphilic character to NCs, which became crucial for the effective interaction with bacterial envelopes. Therefore, MIC and MBC values of FcCAR@Ag NCs against *Staphylococcus aureus* and *Escherichia coli* demonstrated the superior antimicrobial efficacy of silver in nanocluster form compared with conventional silver ions ($AgNO_3$). Specifically, a two-fold reduction of MIC (from 11.7 to 5.8 μg mL^{-1} for *S. aureus* and from 5.8 to 2.9 μg mL^{-1} for *E. coli*) along with a four-fold reduction in MBC (from 46.7 to 11.7 μg mL^{-1} for *S. aureus* and from 11.7 to 2.9 μg mL^{-1} for *E. coli*) was observed. In addition, low MIC values (5.8 μg mL^{-1}) were found against clinically relevant bacteria, including methicillin-resistant *S. aureus* (MRSA), vancomycin-resistant *Enterococcus faecium* (VREfm), *Pseudomonas aeruginosa*, and ESBLs producing *Escherichia coli*. Moreover, FcCAR@Ag NCs were also effective in reducing biomass and metabolic activity of 24 h-established biofilms formed by *S. aureus*, *E. coli*, and *P. aeruginosa* strains. Overall, our findings highlight the strong antimicrobial potential of FcCAR@Ag NCs against both Gram-positive and Gram-negative bacteria, including antibiotic-resistant and biofilm-producing strains.

Received 15th March 2026,
Accepted 19th May 2026

DOI: 10.1039/d6tb00577b

rsc.li/materials-b

Introduction

Metal nanoclusters (NCs) are a new class of extremely small nanomaterials (1–5 nm) with remarkable properties such as intrinsic tunable photoluminescence (PL), large Stokes-shift, great photostability, biocompatibility, and antimicrobial activity. Notably, their optical and functional properties remain stable not only in colloidal dispersions but also in the solid state, further enhancing their versatility. The development of NCs with an innovative architecture has been widely exploited in the

[a] *Interdisciplinary Research Institute in Bio-Nano-Sciences, Babes-Bolyai University, T. Laurian Str. 42, 400271 Cluj-Napoca, Romania*
[b] *Department of Chemical, Biological, Pharmaceutical and Environmental Sciences, University of Messina, V.le F. Stagno d'Alcontres 31, 98166 Messina, Italy. E-mail: apiperno@unime*
[c] *National Research Council, Institute for Nanostructured Materials (CNR-ISMN), URT of Messina at Dept. of Chemical, Biological, Pharmaceutical and Environmental Sciences (ChiBioFarAm), University of Messina, Viale F. Stagno d'Alcontres 31, 98166 Messina, Italy*
[d] *Nanotech Solutions, Ctra Madrid 23, 40150 Villacastín, Spain*
[e] *Faculty of Nursing and Health Sciences, Iuliu Hatieganu University of Medicine and Pharmacy, Victor Babeş 8, RO-400012 Cluj-Napoca, Romania*

interdisciplinary nanotechnology research area for their cutting-edge applications in energy storage, catalysis, sensing, and biomedical fields.[1–7] NCs include different nanostructures composed of a metal core (*e.g.*, gold, silver, platinum, and copper) stabilized by a shell of organic ligands that tailor their solubility, stability, and surface reactivity.[8] Their preparation exploits different strategies, including microwave-assisted, sonochemical, photoreductive, etching-based, or template-assisted protocols.[9] Kinetically controlled syntheses that employ large excesses of proteins or peptides as templates are considered the preferred chemical strategies for preparing NCs in nanomedicine. Several proteins or peptides, such as bovine serum albumin, lysozyme, globulins, carnosine, and glutathione, have been investigated for the preparation of noble metal NCs, however the role of the specific amino acid in the peptidyl backbone is still not clear. Gold nanoclusters (Au NCs) have been extensively studied due to their relatively robust formation and stability in aqueous solutions.[10,11] In contrast, the synthesis of silver nanoclusters (Ag NCs) presents notable challenges, primarily owing to the high susceptibility of silver ions to reduction and subsequent oxidative degradation under ambient conditions. This instability complicates the reproducibility and scalability of Ag NCs synthesis, requiring careful control of reaction parameters and ligand selection.[12,13] In the present study, we report a straightforward chemical strategy for the conversion of silver nitrate into silver nanoclusters (FcCAR@Ag NCs, Fig. 1) using the amphiphilic ferrocene-carnosine ligand (FcCAR).[14]

Short peptides containing the ferrocene unit endowed with peculiar sensing properties have been reported in the literature, including Fc-Gly-Ala developed for sensing of divalent ions; Fc-His-His, a ratiometric peptide responding to fluorescence and pH external stimulus;[15] and FcCAR (Fc-βAla-His) developed by our group for the electrochemical sensing of manganese[14] and mercury[16] (Fig. 1). In the present work, the electrochemical properties of FcCAR were further exploited for the chemical reduction of silver ions into silver nanoclusters (FcCAR@Ag NCs). The increasing prevalence of antibiotic-resistance and the high tolerance of biofilm-associated infections to conventional antibiotics underscore the need for the development of novel and effective alternatives. The use of FcCAR provided, in high yield, colloidally stable Ag NCs endowed with strong antibacterial activity against both Gram-positive and Gram-negative bacteria, including antibiotic-resistant and biofilm-producing strains. Due to their intriguing physicochemical properties, such as the core size (2.75 ± 0.35 nm), surface charge (−25.3 ± 4.8 mV), amphiphilic nature of the ligand, and remarkable antimicrobial properties, FcCAR@Ag NCs could be embraced in the emergent family of ultrasmall silver particles active against multi-drug-resistant (MDR) bacteria.[3,17–19] The benefit of ultra-small silver particles as antibacterial agents over the commercially available silver nanoparticles (Ag NPs) was investigated by Xie and co-workers.[3] They fabricated silver particles reaching the Ångstrom scale by a physical approach. After fructose coating, the naked AgÅPs (14.43 ± 8.14 Å) were converted into nanosized F-AgÅPs (9.09 ± 3.27 nm), suitable for intravenous use, and more effective against *S. aureus* MDR strain than Ag NPs.

Moreover, injection solutions of F-AgÅPs were investigated for treating lung, pancreatic, osteosarcoma, melanoma, and gastric cancers in animal models, and the observed antitumor effects were ascribed to several mechanisms of action, inducing damage to the cellular ultrastructure, ROS upregulation, DNA damage, and promotion of CD8+T cell infiltration.[20,21]

On the other hand, Ag NCs covered by cationic capping agents showed enhanced bactericidal effects due to electrostatic interactions with negatively charged bacterial membranes.[22] Haidari *et al.* developed a green procedure for the preparation of polycationic silver nanoclusters (pAg NCs) using chitosan as a reducing and stabilizing agent.[18] From this study emerged the ability of pAg NCs to eradicate both Gram-positive and Gram-negative bacteria in their planktonic form, as well as their corresponding established multispecies biofilms. The cationic nature of pAg NCs, together with their small core size (2.5 ± 0.46 nm), facilitated the penetration of the bacterial cell membrane, while the high percentage (>50%) of silver ions on the cluster surface acted as the Ag^+ nanoreservoir. The superior antimicrobial activity against MDR bacteria of amphiphilic small-sized AgNCs with respect to conventional Ag NPs was also demonstrated by Chen *et al.*[17] The reported experimental data and MD simulation findings suggested that the amphiphilic ligands on AgNC surfaces promoted the interactions with bacterial cells through active endocytosis pathways. Despite these promising literature results, the development of antimicrobial nanomedicine based on Ag NCs is still confined to the laboratory arena. Further efforts by advanced nanocluster chemistry should empower the fine-tuning of surface ligands to produce Ag NCs with precise size, composition, and surface properties to unveil the correlation between physical–chemical properties of AgNCs and biological activity. Moreover, the coexistence of multiple and interconnected optical, catalytic, and electrochemical[23] properties makes metal NCs appealing for advanced technological applications that can include the development of electroactive antibacterial systems, as well as the design of hybrid and nanocomposite materials for the modification of electrode surfaces with well-defined molecular interfaces.[23–25] In this context, we report the development of ultrasmall FcCAR@Ag NCs decorated with the amphiphilic

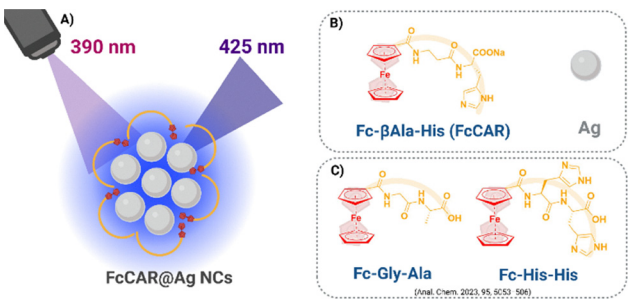

Fig. 1 Sketched view of FcCAR@Ag NCs and their photoluminescence properties reported in this work (A). Chemical structure of amphiphilic ferrocene-β-Ala-His (FcCAR) (B), Fc-Gly-Ala, and Fc-His-His (C) ligands.[15] Created with Biorender.com.

dipeptide FcCAR (Fc-β-Ala-His, Fig. 1). This ligand is a derivative of L-carnosine (β-Ala-His), a naturally occurring dipeptide with a non-enzymatic free-radical scavenger activity. The conjugation of the amine group of the β-Ala residue with ferrocenyl carboxylic acid produces a redox-active ligand with electron-transfer properties that has been exploited in the present work for the eco-friendly synthesis of Ag NCs.[26] Specifically, FcCAR acted as a reducing and stabilizing agent in the synthesis of FcCAR@Ag NCs, conferring amphiphilic properties to the surface of Ag NCs. The photoluminescence and electrochemical properties of FcCAR@Ag NCs were investigated and compared with those of the native FcCAR ligand. The electrochemical behavior of FcCAR@Ag NCs and FcCAR was compared on two types of screen-printed electrodes (SPEs) using cyclic voltammetry (CV). FcCAR@Ag NCs also showed a reversible redox process on both SPEs used and a peak anodic current almost double that of native FcCAR on screen-printed carbon electrodes (SPCEs). The enhanced electrochemical response relative to the anodic signal was also evident in differential pulse voltammetry (DPV). The antimicrobial efficiency of FcCAR@Ag NCs was evaluated against Gram-positive and Gram-negative bacteria in their planktonic form, and the activity was compared with silver nitrate, a topical antiseptic approved in several country pharmacopoeias for the cauterization of superficial hemorrhages or to refresh ulcers.[27] Moreover, the effect of FcCAR@Ag NCs on biomass and metabolic activity of 24 h-established biofilms of *Staphylococcus aureus*, *Escherichia coli*, and *Pseudomonas aeruginosa* strains was evaluated.

Experimental

Materials and methods

Ferrocene-β-Ala-His (FcCAR) was synthesized according to the literature.[26] Silver nitrate ($AgNO_3$), ascorbic acid (AA), and sodium hydroxide (NaOH) were purchased from Merck (Italy). Potassium chloride (KCl, extra pure) was purchased from Sigma-Aldrich.

Characterization

UV/vis spectra were obtained on a model Jasco V-730 using 1 cm path length quartz cells at r.t. ≅25 °C. Steady-state fluorescence spectroscopy measurements were performed on a Jasco model FP-750 spectrofluorometer by using a 1 cm path length quartz cell. Fluorescence lifetime decay curves of the substrate (FcCAR) and FcCAR@Ag NCs were obtained using a time-resolved confocal fluorescence MicroTime 200 microscope system from PicoQuant (Berlin, Germany). The measurements were performed under a 405 nm excitation laser (PicoQuant diode laser LDH-D-C-405, 40 MHz). The absolute quantum yield (QY) was acquired under an excitation of 400 nm *via* a JASCO spectrofluorometer FP-8600 equipped with an integrating sphere accessory (ILF-835) in a 3 mm thickness quartz cuvette. The mean hydrodynamic diameter (D_H) and zeta-potential (ζ) were measured through photon correlation spectroscopy (PCS) with a Zetasizer Nano ZS (Malvern Instrument, Malvern, UK) at 25 °C in ultrapure water. The measurements were performed at a 173° angle with respect to the incident beam at 25 ± 1 °C for each dispersion. The deconvolution of the measured correlation curve to an intensity size distribution was achieved by using a non-negative least-squares algorithm. The ζ-potential values were determined using a Zetasizer Nano ZS Malvern Instrument equipped with a He–Ne laser at a power P = 4.0 mW and λ = 633 nm. The results are reported as the mean of three separate measurements on three different batches ± the standard deviation (SD). TGA was performed using an SDT650 (TA Instruments). The measurements were performed in a nitrogen atmosphere (100 mL min^{-1}), in the 80–750 °C range with a thermal ramp of 10 °C min^{-1}. Transmission electron microscopy analyses were carried out using a Jeol JEM-1010 microscope equipped with a CMOS 4K × 4K, F416 de TVIPS camera. X-ray photoelectron spectroscopy (XPS) was performed using a SPECS PHOIBOS 150MCD system featuring a 250 W monochromatic Al Kα source, a hemispherical analyzer, and a multichannel detector. To ensure data integrity, the analysis chamber vacuum was maintained between 10^{-10} and 10^{-9} mbar. Binding energies were calibrated using the C 1s peak at 284.6 eV as an internal charge reference. Surface elemental compositions were derived from survey spectra (0–1200 eV) *via* standard quantitative analysis. High-resolution spectra were acquired at a 30 eV pass energy, with peak fitting performed after applying Shirley-type background subtraction.

All electrochemical measurements were performed in KCl (0.1 M) aqueous solutions using a PC-controlled electrochemical workstation (μAutolab potentiostat–galvanostat type III (Eco Chemie)), interfaced with a three-electrode cell configuration (Metrohm DropSens SPE, DRPDSC4MM 72098). Two types of SPEs were used, *i.e.* screen-printed carbon electrodes (SPCEs, DRP-110) and screen-printed platinum electrodes (Pt-SPE, DRP-550). While SPCEs consist of carbon working and auxiliary electrodes, and a silver reference electrode (RE), Pt-SPEs are based on platinum working and auxiliary electrodes and a silver RE. Voltammograms were deconvoluted using a general purpose electrochemical system (GPES), version 4.9, by using Eco Chemie B.V. processing software. The redox properties of FcCAR@Ag NCs (1 mM) in KCl (0.1 M) were evaluated by CV and DPV in the potential range from −0.4 V to +0.8 V (*vs.* Ag), and compared with the electrochemical behavior of FcCAR (1 mM) in KCl (0.1 M). CV was performed over a wide range of scan rates ($0.005 \leq \nu/V\ s^{-1} \leq 0.500$) at 0.1 V s^{-1}, and DPV measurements were carried out with a potential step and amplitude of 0.010 V and 0.1 V, respectively.

Synthesis of silver nanoclusters

All the glassware was carefully cleaned with aqua regia (HCl/HNO_3, volume ratio 3 : 1) and rinsed thoroughly with ultrapure water before use. Ligand stock solutions (FcCAR, 100 mM; 46 mg mL^{-1}), $AgNO_3$ (5 mM), ascorbic acid (AA, 50 mM), and NaOH (1 M) were prepared using ultrapure water. Optimized FcCAR@Ag NCs were prepared according to experimental conditions described as entry 1: to the FcCAR stock solution (3 mL, 0.3 mmol), pre-heated at 80 °C, the $AgNO_3$ stock solution

(1 mL, 0.005 mmol) was added under stirring. After 5 minutes, AA (50 mM, 0.02 mL) was added, and the pH was corrected by the addition of 0.5 mL of 1 M NaOH (pH ~ 11.5). The mixture was stirred for 4 h at 80 °C and then cooled to room temperature. The batch-to-batch reproducibility was evaluated by assessing the photoluminescence, colloidal stability, and MIC values of samples across different batches produced at different times. The FcCAR@Ag NCs water solution was stored at 4 °C and used without purification. The nominal contents of FcCAR and silver in FcCAR@Ag NCs solution are 66 mM (30.36 mg mL^{-1}) and 1.1 mM (119 μg mL^{-1}), respectively.

Antibacterial activity

The microorganisms used in this study were clinically relevant bacteria, namely *Staphylococcus aureus* ATCC 6538, methicillin-resistant *S. aureus* (MRSA) ATCC 43300, vancomycin-resistant *Enterococcus faecium* (VREfm) DSM 17050, *Escherichia coli* ATCC 10536, extended-spectrum β-lactamases (ESBLs) producing *E. coli* DSM105388, and *Pseudomonas aeruginosa* ATCC 9027. Minimal inhibitory concentration (MIC) and the minimal bactericidal concentration (MBC) of the FcCAR@Ag NCs were performed according to the guidelines of the Clinical and Laboratory Standards Institute (CLSI),[28] with some modifications. The samples were twofold diluted in 96-well round-bottomed plates using Mueller–Hinton broth (MHB), and overnight bacterial cultures were inoculated to yield a final concentration of 5×10^5 CFU mL^{-1}. After incubation at 37 °C for 24 h, the MBC was determined by seeding 20 μL from all clear wells onto Mueller–Hinton agar and incubating at 37 °C for 24 to 48 h. The MBC was defined as the lowest concentration that killed 99.9% of the inoculum. The data from at least three replicates were evaluated, and the modal results were calculated.

Effect on preformed 24 h-biofilms

Overnight cultures grown in tryptic soy broth (TSB) or TSB + 1% glucose (*S. aureus*) were standardized to 1×10^6 CFU mL^{-1} and were inoculated (100 μL) in 96-well polystyrene flat-bottomed microtiter plates. After incubation for 24 h at 37 °C, the planktonic bacterial growth was dislodged, and the wells were washed with sterile PBS and filled with twofold dilutions of samples, ranging from the MIC to an 8-fold the MIC (referred to the values reported in Table 5). After incubation for 24 h at 37 °C, the effects on: (i) biofilm biomass and (ii) biofilm metabolic activity were estimated.

(i) Biofilm biomass: the planktonic growth was dislodged, and each well was washed with PBS, dried, stained with 0.1% safranin, and then washed with water; the biofilm biomass was eluted in acetic acid 30% (v/v), and OD492 was quantified.

(ii) Biofilm metabolic activity: the planktonic growth was dislodged and, after washing, each well was treated with the Cell Proliferation Kit II XTT (Roche Diagnostics, Mannheim, Germany) as previously reported.[29] This assay is based on the metabolic reduction of a tetrazolium salt [2,3-bis[methyloxy-4-nitro-5-sulfophenyl]-2*H*-tetrazolium-5-carboxanilide (XTT)] to a colored water-soluble formazan derivative. Briefly, each well was filled with the XTT solution (final concentration 0.3 mg mL^{-1}) for 5 h at 37 °C, and the formazan derivative was measured spectrophotometrically at 492 nm. The reduction of biofilm biomass and biofilm metabolic activity was estimated using eqn (1).

$$\left[100 - \frac{(OD_{492\,\text{of treated well}} - OD_{\text{blank}})}{(OD_{\text{con 492 of control}} - OD_{\text{blank}})}\right] \times 100 \qquad (1)$$

Statistical analysis

Results were expressed as the mean ± standard deviation (SD) from three experiments. A two-way analysis of variance (ANOVA) was used to determine significant differences between the samples after treatment. Multiple comparisons were performed among groups using the Bonferroni correction test. The results with a p-value < 0.05 were considered statistically significant.

Results and discussion

Synthesis of amphiphilic silver nanoclusters (FcCAR@Ag NCs)

Nanoclusters were synthesized in a one-step template-assisted method by adding silver ions to the pre-heated aqueous solution containing the FcCAR ligand in large excess and in the presence of ascorbic acid as a mild reducing agent (Fig. 2). The reaction was carried out under basic conditions (pH ~ 11.5), according to the literature, to promote efficient nanocluster formation and stabilization.[12] Under these experimental conditions, the main functional groups of FcCAR are in a deprotonated form,[26] favoring coordination with silver ions.

Several attempts to optimize the photoluminescence (PL) properties of NCs were carried out (Table 1) by varying the ligand/metal ratio (L/Me), temperature (T), and reaction time. The best PL properties were obtained using the experimental conditions described as entry 1 (Table 1). Briefly, a concentrated aqueous solution of the ligand (100 mM) pre-heated to 80 °C was mixed with $AgNO_3$ aqueous solution (5 mM) under stirring. Ascorbic acid (50 mM) was added to assist the reduction of silver ions, and the pH was corrected by NaOH addition. The samples prepared at a lower L/Me molar ratio (*e.g.*, FcCAR/Ag^+ 6.25 : 1, entry 2, Table 1) showed PL properties lower than those of the entry 1. Moreover, to investigate the role of ferrocene units on the formation of Ag NCs, the entry 1 protocol was applied to unmodified CAR: despite the higher

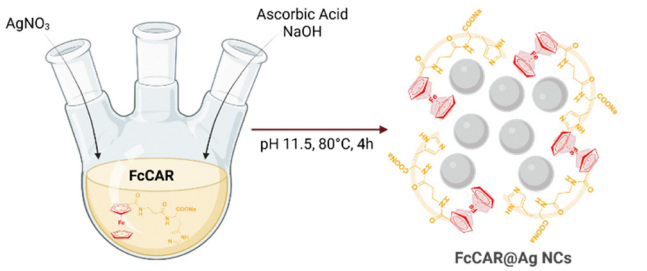

Fig. 2 Schematic representation of FcCAR@Ag NCs synthesis. Created with Biorender.com.

Table 1 Experimental conditions investigated for silver NC preparation

Entry	Ligand	L/Me	*T*/time, pH	Results
1	FcCAR	62.5/1	80 °C/4 h, pH 11.5	NCs with maximum PL intensity
2	FcCAR	6.25/1	80 °C/4 h, pH 11.5	NCs with good PL intensity
3	FcCAR	62.5/1	80 °C/12 h or 40 °C/4 h, pH 11.5 or pH 7.5	Products with weak PL properties and/or formation of Ag NPs and metallic Ag
4	CAR	62.5/1	80 °C/4 h, pH 11.5	Products with poor PL properties

ligand excess and the presence of ascorbic acid no products with measurable PL were detected (entry 4, Table 1), pointing out the linchpin role of the ferrocene unit that increases the reducing capacity of the natural dipeptide, enabling the formation of nanoclusters containing the metals in dominantly zero oxidation state. Moreover, complete batch-to-batch reproducibility was observed for the synthetic protocol described in entry 1. No evident changes in the key properties of FcCAR@Ag NCs (*e.g.*, photoluminescence, colloidal stability, size, and antimicrobial activity) were documented for FcCAR@Ag NCs samples produced at different times.

Physicochemical characterization

The amphiphilic FcCAR@Ag NCs were characterized by transmission electron microscopy (TEM) analyses and by their peculiar optical properties. FcCAR@Ag NCs exhibited spherical-shaped morphology and a narrow particle size distribution with a mean diameter of 2.75 ± 0.35 nm (Fig. 3). The mean hydrodynamic diameter (D_H) of FcCAR@Ag NCs measured in water by dynamic light scattering (DLS, Table 2) showed a value of ~45 nm, which could likely be ascribed to the presence of NCs embedded in the matrix of FcCAR aggregates. Indeed, aggregation of FcCAR is suggested by the D_H value (Table 2), according to the literature reporting the same behavior for BSA-stabilized AuNCs.[30] Negative ζ-potential (−25.3 mV, Table 2) ensured high colloidal stability of FcCAR@Ag NCs. Thermogravimetric analysis (TGA) confirmed that the surface of Ag NCs was passivated by FcCAR, with ~48.5% of the contribution coming from the ligand only (Fig. S1); the latter not only protected Ag NCs in solution but also provided outstanding thermal stability according to the literature.[18]

Table 2 Mean hydrodynamic diameter (D_H) and zeta potential (ζ) in ultrapure water

Sample	D_H (nm ± SD)[ab] (%)	ζ (mV ± SD)
FcCAR@Ag NCs	45.4 ± 5.45 (100)	−25.3 ± 4.8
FcCAR	104 ± 28 (90), 440 ± 16 (10)	−11.7 ± 4.7

[a] SD was calculated from three different batches. [b] Size with corresponding number % distribution. [FcCAR] = 2.3 mM.

The formation of ultrasmall Ag NCs was suggested by both the intrinsic blue PL observed under UV irradiation (Fig. S2) and the absence of any significant surface plasmon resonance band in the range 400–450 nm in the UV/vis spectrum.[31] Then, the peculiar intrinsic PL properties of FcCAR@Ag NCs were assessed through comprehensive spectroscopic characterization that included UV/vis and excitation/emission spectra (Fig. 4A, B and Fig. S3) and the determination of the absolute quantum yield (QY%) value. The UV/vis absorption spectrum (Fig. 4A) exhibits the ligand bands at around 263 nm and 306 nm, and a shoulder peak at around 345 nm for both FcCAR and FcCAR@Ag NCs, attesting to the functionalization of Ag NCs with the carnosine derivative. It is well-known that amino acids conjugated with ferrocene can form amphiphilic structures with emission properties tunable through their aggregation behavior.[15,32] FcCAR@Ag NCs showed high fluorescence emission at 425 nm by excitation at 390 nm, whereas a weak emission was detected for the FcCAR ligand under the same experimental conditions (Fig. 4B) although it could produce fluorescent nanoaggregates.[15] We hypothesize that an increased aggregation-induced emission could occur by the arrangement of FcCAR amphiphiles around Ag NCs.

Emission properties of FcCAR@Ag NCs were confirmed using fluorescence emission spectra at different excitation wavelengths (Fig. 5) and using excitation spectra at λ_{em} = 425 nm (Fig. S3), which revealed that the emission bands are due to the electronic transition of the FcCAR ligand in the 260–280 nm range.

To quantify the luminescence efficiency, the absolute quantum yield (QY%) of FcCAR@Ag NCs was determined using a JASCO integrating sphere setup. The QY of the blue-emitting nanoclusters was measured to be 5.9%, a relatively high value for ligand-stabilized silver nanoclusters in aqueous media.

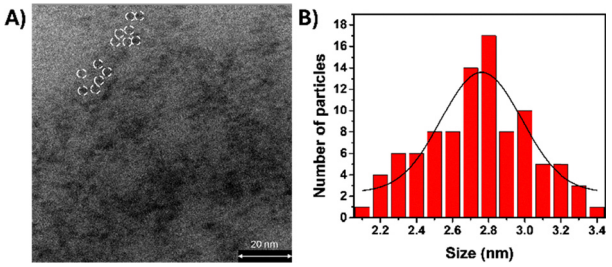

Fig. 3 TEM image (scale bar: 20 nm) (A) and size distribution (B) of FcCAR@Ag NCs.

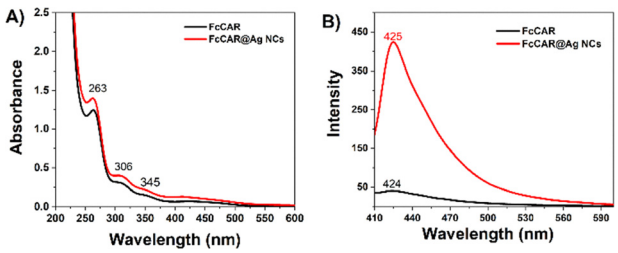

Fig. 4 UV/vis (A) and fluorescence emission (B) spectra of FcCAR ([FcCAR] = 220 μM,) and FcCAR@Ag NCs (path length = 1 cm, λ_{exc} = 390 nm).

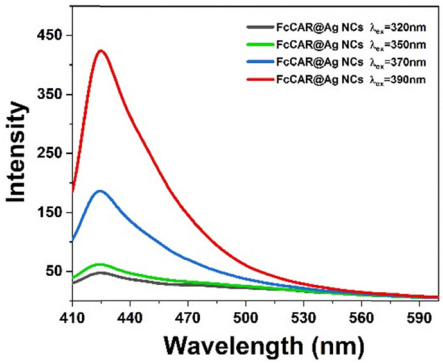

Fig. 5 Fluorescence emission spectra of FcCAR@Ag NCs at different excitation wavelengths.

This result underscores the effectiveness of FcCAR not only as a stabilizing agent but also as a photophysically active scaffold that enhances emission through its amphiphilic and electron-donating ferrocene moiety. To gain further insight into the excited-state dynamics of the FcCAR ligand and FcCAR@Ag NCs, fluorescence lifetime measurements were performed, and the time-resolved fluorescence decay profiles are reported in Fig. 6. The fluorescence three-component lifetimes (Table 3) were calculated using tail-fit fitting operations until the standard deviation, the residues, and χ^2 converged to optimal values. Following the formation of Ag NCs, a slight decrease in the average fluorescence lifetime was observed, from 4.58 ns for FcCAR to 3.51 ns for FcCAR@Ag NCs. This reduction is primarily attributed to a significant decrease in the long-lived component τ_1, which dropped from 7.2 ns to 5.0 ns upon Ag NCs formation. This acceleration of decay suggests that the electronic environment of the ligand has been fundamentally changed. Such a transition is characteristic of a move from purely molecular relaxation to a cluster-centered emission. In noble metal nanoclusters, this optical behavior is typically governed by ligand-to-metal charge transfer (LMCT) or ligand-to-metal–metal charge transfer (LMMCT) processes. In this framework, the electron-rich carnosine derivative acts as a donor shell, while the silver core provides a high density of states that facilitates new, efficient radiative pathways *via* electronic coupling. The ferrocene moiety plays an integral role

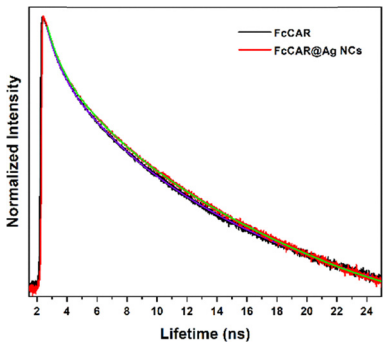

Fig. 6 Fluorescence lifetime–decay curves of FcCar (green line) and FcCAR@Ag NCs (black line).

Table 3 The fluorescence three-component lifetimes

Sample	t_1 (ns)	I_1 (%)	t_2 (ns)	I_2 (%)	t_3 (ns)	I_3 (%)	t_{av} int (ns)
FcCAR	7.2	49.4	2.4	39.9	0.59	10.7	4.58
FcCAR@Ag NCs	5.0	47.6	2.5	44.3	0.68	8.2	3.51

here: beyond its synthetic contribution to silver ion reduction, it likely modulates the electronic density at the metal–ligand interface, thereby promoting the LMMCT pathway. This sophisticated photophysical synergy is ultimately reflected in the relatively high absolute quantum yield of 5.9%, which highlights the efficiency of the charge-transfer processes within the FcCAR-stabilized architecture.

XPS analysis was carried out to determine the elemental composition of FcCAR and FcCAR-Ag NCs and gain deeper insight into the interaction between Ag NCs and FcCAR ligands. The survey spectra, the valence band (VB) and core level C 1s, O 1s, N 1s, Fe 2p, and Ag 3d spectra, along with their corresponding peak-fitting results for both samples, are presented in Fig. 7 and Fig. S5 and S6. According to literature data, the binding energies of Ag 3d5/2 and Ag 3d3/2 for metallic silver were detected at 368.6 and 374.7 eV, respectively.[33]

Electrochemical investigation

The electrochemical behavior of FcCAR@Ag NCs (1 mM) in KCl (0.1 M) was first studied on SPEs (SPCE and Pt-SPCE), performing CV analyses at 0.1 V s^{-1}, and was compared with native FcCAR (1 mM) in KCl (0.1 M). Fig. 8A reports the relative scans along with the CVs on SPCE and Pt-SPE. Both FcCAR and FcCAR@Ag NCs display a reversible redox process on the two types of SPEs. The anodic and cathodic peak potentials ($E_{a,p}$, $E_{c,p}$) of FcCAR and FcCAR@Ag NCs, along with their anodic and cathodic peak currents ($i_{a,p}$, $i_{c,p}$), on both SPEs, are reported in Table 4. As for peak currents, Fig. 8 shows an increase in capacitive current on Pt-SPE; consequently, the peak current values are slightly higher on this electrode than those obtained on the SPCE (Table 4). The $i_{a,p}$ value of FcCAR@Ag NCs increases by ~43% on SPCE, compared to that of FcCAR, and by ~17% on Pt-SPE. This trend in the anodic response of FcCAR@Ag NCs on SPCE is also visible in DPV, as reported in Fig. 8B, which highlights a peak increase of 64.4% on SPCE, compared to 25.5% on Pt-SPE. Further CV analyses were conducted on SPCE to gain deeper insight into the electrochemical behavior of FcCAR and FcCAR@Ag NCs. The corresponding

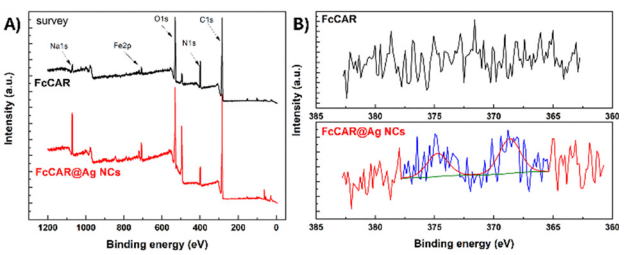

Fig. 7 (A) XPS survey spectra and (B) Ag3d spectra of FcCAR and FcCAR@Ag NCs.

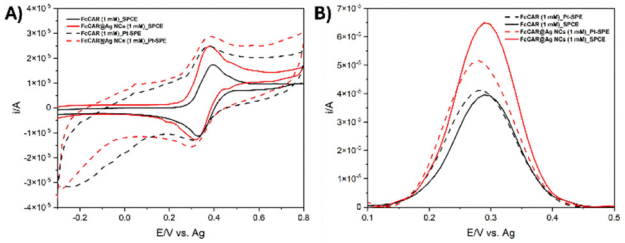

Fig. 8 (A) Scans in CV of FcCar (1 mM) in KCl (0.1 M, black lines) and FcCAR@Ag NCs (1 mM) in KCl (0.1 M, red lines) on SPCE (solid lines) and on platinum screen-printed electrode (Pt-SPE, dashed lines). (B) Scans in DPV of FcCAR (1 mM) in KCl (0.1 M, black lines) and FcCAR@Ag NCs (1 mM) in KCl (0.1 M, red lines) on SPCE (solid lines) and on platinum screen-printed electrode (Pt-SPE, dashed lines).

Table 4 Electrochemical values ($E_{a,p}$, $E_{c,p}$, $i_{a,p}$, $i_{c,p}$) of FcCar and FcCAR@Ag NCs on SPEs

Sample	$E_{a,p}$/V *vs.* Ag	$i_{a,p}$/μA	$E_{c,p}$/V *vs.* Ag	$i_{c,p}$/μA
SPCE				
FcCAR	0.394	17.5	0.331	11.5
FcCAR@Ag NCs	0.376	25.1	0.314	12.9
Pt-SPE				
FcCAR	0.376	24.9	0.316	13.2
FcCAR@Ag NCs	0.376	29.1	0.316	15.2

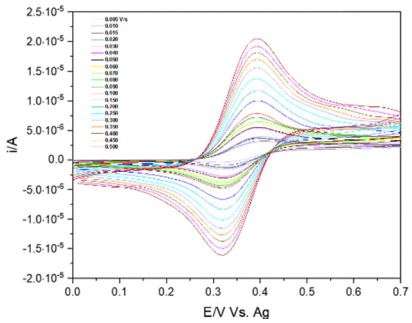

Fig. 9 CV scans of FcCAR@Ag NCs (1 mM) in KCl (0.1 M) on SPCE at different scan rate values ($0.005 \leq \nu/V\ s^{-1} \leq 0.500$).

CV scans are presented in Fig. S7 and Fig. 9, respectively. The anodic peak potential ($E_{a,p}$) and cathodic peak potential ($E_{c,p}$) of both FcCAR and FcCAR@Ag NCs remained nearly unchanged, with a peak-to-peak separation (ΔE) of approximately 0.060 V across different scan rates (Fig. S8). This behavior indicates a reversible one-electron redox process controlled by diffusion.[34,35]

The electroactive surface area A was calculated according to the Randles–Ševčik equation (see SI). The increase in A value for FcCAR@Ag NCs is consistent with the presence of NCs on the electrode surface, which increases the surface-to-volume ratio and introduces a large number of active sites. This factor, along with the assembly of FcCAR on the NCs surface, may underlie the enhanced electron transfer efficiency and highlight the potential of FcCAR@Ag NCs in electroanalytical applications.[23]

Antibacterial activity

The antibacterial activity of silver in the nanocluster form was initially assessed against the planktonic forms of *S. aureus* (ATCC 6538) and *E. coli* (ATCC 10536), using silver ions from silver nitrate as positive controls. FcCAR@Ag NCs exhibited MIC values of 5.8 and 2.9 μg mL^{-1} and MBC values of 11.7 and 2.9 μg mL^{-1} against *S. aureus* and *E. coli*, respectively (Table 5). Overall, the comparison of MIC and MBC values highlights the superior antimicrobial performance of silver in nanocluster form compared with conventional silver ions ($AgNO_3$), showing a twofold reduction in MIC (from 11.7 to 5.8 μg mL^{-1} and from 5.8 to 2.9 μg mL^{-1}) and a four-fold reduction in MBC (from 46.7 to 11.7 μg mL^{-1} and from 11.7 to 2.9 μg mL^{-1}) for both strains. Consistently, the enhanced activity typically associated with silver against Gram-negative bacteria was evident for both forms of silver (*i.e.* ions and nanoclustered species). Subsequently, the evaluation of the antimicrobial efficacy of silver in the nanocluster form was extended to other four important bacterial strains selected for their pathogenicity and antibiotic-resistance profiles: the Gram-positive strains methicillin-resistant *Staphylococcus aureus* (MRSA) ATCC 43300 and vancomycin-resistant *Enterococcus faecium* (VREfm) DSM 17050, and the Gram-negative strains *Pseudomonas aeruginosa* ATCC 9027 and extended-spectrum β-lactamases (ESBLs) producing *Escherichia coli* (DSM 105388). A low MIC value of 5.8 μg mL^{-1} was also found for these clinically relevant bacteria. Comparison of FcCAR@Ag NCs with clinically relevant antibiotics (Table S7) showed MIC values ranging from 2.9 to 5.8 μg mL^{-1} against all tested strains. In contrast, vancomycin, a glycopeptide active against Gram-positive bacteria, was effective only against the two *S. aureus* strains (MIC = 1 μg mL^{-1}), while ciprofloxacin exhibited broader activity against both Gram-positive and Gram-negative bacteria (MIC = 0.125–0.5 μg mL^{-1}), except for the resistant *E. coli* DSM 105388 (MIC = 8 μg mL^{-1}). These results highlight the promising broad-spectrum activity of the NCs against both Gram-positive and Gram-negative bacteria.

The MBC values demonstrated the notable bactericidal effect of the Ag nanocluster against Gram-negative strains (MBC of 5.8 μg mL^{-1}), whereas reduced killing activity was observed against Gram-positive bacteria (MBC = 23.4 and

Table 5 MIC and MBC values of silver in nanocluster form (FcCAR@Ag NCs) and in conventional silver ions ($AgNO_3$) against Gram-positive and Gram-negative bacteria

Bacteria	Sample	MIC[a] (μg mL^{-1})	MBC[a] (μg mL^{-1})
S. aureus ATCC 6538	FcCAR@Ag NCs	5.8	11.7
	$AgNO_3$	11.7	46.7
E. coli ATCC 10536	FcCAR@Ag NCs	2.9	2.9
	$AgNO_3$	5.8	11.7
S. aureus (MRSA) ATCC 43300	FcCAR@Ag NCs	5.8	23.4
E. faecium (VREfm) DSM 17050	FcCAR@Ag NCs	5.8	46.7
E. coli DSM 105388	FcCAR@Ag NCs	5.8	5.8
P. aeruginosa ATCC 9027	FcCAR@Ag NCs	5.8	5.8

[a] Expressed as $AgNO_3$ concentration.

46.7 μg mL^{-1}). No activity was detected for the FcCAR ligand at the highest tested concentration (33 mM, 15.2 mg mL^{-1}).

FcCAR@Ag NCs showed a significant efficacy ($p < 0.05$) on the *S. aureus* biofilm, even at concentrations slightly higher than those active on the planktonic phase (11.7 μg mL^{-1} = 2 × MIC). Specifically, the effective percentage reduction of biofilm biomass (47%, 65%, 68%) and metabolic activity (46%, 71%, and 74%) was detected at 11.7 μg mL^{-1} (2 × MIC), 23.4 μg mL^{-1} (4 × MIC), and 46.8 μg mL^{-1} (8 × MIC), respectively.

A smaller effect of FcCAR@Ag NCs on *E. coli* and *P. aeruginosa* biofilms was observed (Fig. 10). At doses equal to 8 × MIC, a decrease of 54% and 62% of biomass, and 39% and 37% of metabolic activity, respectively, was detected. However, it should be highlighted that *E. coli* showed the lowest MIC values (2.9 μg mL^{-1}) compared to other bacteria (5.8 μg mL^{-1}). Consequently, the dose of 8 × MIC corresponded to the dose of 4 × MIC for *S. aureus* and *P. aeruginosa.* Bacteria organized into biofilm communities are a major cause of nosocomial and community-acquired infections due to their tolerance to conventional antibiotics and host immune defenses. Therefore, the development of novel approaches to effectively combat biofilm-associated infections is required. The results of this study demonstrated that FcCAR@Ag NCs affected the structure and physiology of established biofilms. Specifically, FcCAR@Ag NCs showed a comparable reduction in total biomass and metabolic activity of *S. aureus* biofilms, indicating a coordinated impact on both biofilm architecture and bacterial physiology.

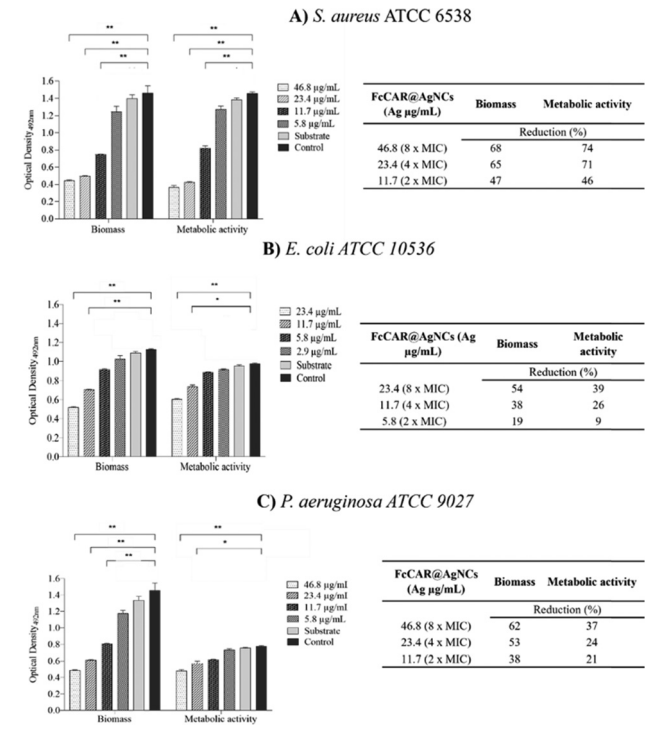

FcCAR@AgNCs (Ag μg/mL)	Biomass	Metabolic activity
	Reduction (%)	
46.8 (8 x MIC)	68	74
23.4 (4 x MIC)	65	71
11.7 (2 x MIC)	47	46

FcCAR@AgNCs (Ag μg/mL)	Biomass	Metabolic activity
	Reduction (%)	
23.4 (8 x MIC)	54	39
11.7 (4 x MIC)	38	26
5.8 (2 x MIC)	19	9

FcCAR@AgNCs (Ag μg/mL)	Biomass	Metabolic activity
	Reduction (%)	
46.8 (8 x MIC)	62	37
23.4 (4 x MIC)	53	24
11.7 (2 x MIC)	38	21

Fig. 10 Effects of different concentrations (from MIC to 8 × MIC) of FcCAR@Ag NCs on 24 h-biofilms of *S. aureus* (A), *E. coli* (B), and *P. aeruginosa* (C). All data are presented as mean ± SD (* $p < 0.05$; ** $p < 0.01$).

Conversely, in *E. coli* and *P. aeruginosa* biofilms, a more pronounced reduction in total biomass than in metabolic activity was observed, suggesting a preferential effect on biofilm structure rather than on bacterial viability.

Overall, these results revealed a growth-state-dependent behavior of the NCs, with Gram-negative bacteria being more susceptible in the planktonic state, whereas Gram-positive *S. aureus* showed higher susceptibility under biofilm conditions. The greater sensitivity of *E. coli* and *P. aeruginosa* in planktonic form may be related to favorable interactions with the outer membrane and thinner peptidoglycan layer, whereas the opposite trend in biofilms likely reflects differences in nanoparticle penetration and retention within the extracellular polymeric substance (EPS). In this context, the enhanced activity against *S. aureus* suggests a more efficient interaction with the Gram-positive biofilm matrix, leading to improved disruption of biofilm structure and reduced metabolic activity. These findings are consistent with previous reports highlighting that antibiofilm efficacy does not necessarily correlate with planktonic susceptibility but is strongly influenced by nanoparticle–biofilm interactions.[36,37]

The diversity of literature data limits a precise comparison of the properties and performance of FcCAR@Ag NCs with respect to literature Ag NCs. The main obstacles include the lack of uniformity in expressing antimicrobial effect data, the use of not directly comparable antimicrobial and antibiofilm testing protocols that often lack positive control, and the use of different bacterial strains. Nevertheless, based on a general analysis of the literature data, FcCAR@Ag NCs could be included in the restricted family of ultrasmall metal nanoclusters exhibiting strong antimicrobial and antibiofilm activity.[3,10,17–19,38]

The large surface area, the molecular-like physicochemical characteristics, and particularly the presence of amphiphilic functional groups on the surface could confer FcCAR@Ag NCs with superior antibacterial activity compared with conventional silver ions. FcCAR@Ag NCs could act as nanoreservoirs of Ag^+, ensuring a sustained and pharmacologically active concentration of silver ions for effective interaction with bacterial cells.

Stability and biocompatibility of FcCAR@Ag NCs

It is well established that Ag NCs exhibit remarkable stability of their functional properties, particularly photoluminescence, not only in colloidal dispersions but also when immobilized in solid matrices. In this work, the stability of the FcCAR@Ag NCs was evaluated by monitoring the preservation of their key properties after storage at 4 °C for over six months. No differences in electrochemical or antimicrobial properties were observed between fresh and stored FcCAR@Ag samples, as confirmed by antibacterial assays and electrochemical measurements performed at different times (data not shown). Notably, no significant changes in FcCAR@Ag intrinsic photoluminescence were observed, as confirmed by UV/vis absorption and excitation/emission spectra of stored samples (Fig. S4). Moreover, stored FcCAR@Ag NCs maintain their colloidal stability in water and in relevant biologically medium including

Table 6 Mean hydrodynamic diameter (D_H) and PDI of FcCAR@Ag NCs stored at 4 °C for over six months

Medium	D_H (nm ± SD)[a] (%)[b]	PDI
Water	82.36 ± 6.57 (100%)	0.28 ± 0.03
MHB	84.33 ± 19.06 (100%)	0.28 ± 0.03
NaCl	95.03 ± 13.25 (100%)	0.27 ± 0.03
PBS	102.4 ± 4.292 (100%)	0.30 ± 0.02

[a] SD was calculated from three different batches. [b] Size with corresponding number % distribution. [FcCAR] = 2.3 mM.

Mueller–Hinton broth (MHB), NaCl (0.9% wt) and PBS (10 mM pH 7.4) (Table 6). The FcCAR biogenic shell of the reported nanoclusters provided enhanced colloidal stability and ensured solubility in both water and biological media, maintaining these properties even after long-term storage (over six months). DLS analyses indicated particle sizes in the range of 82–102 nm, likely due to different arrangements of the external FcCAR shell aggregates. Unlike literature reports,[12] we observed no metal precipitates or large aggregates in either fresh or stored samples. These results suggested that the increase in DLS size upon storage arises from changes in the peptide shell rather than aggregation of individual clusters.[39]

The biosafety of the as-prepared FcCAR@Ag NCs was evaluated on human skin fibroblast WS1 cells using the PrestoBlue assay (Fig. S9). A cell viability of ≈70% was detected at a concentration of 11.6 μg mL^{-1}, which is two to four times higher than the MIC values (2.9 μg mL^{-1} and 5.9 μg mL^{-1}). Although all MIC values fall in the non-toxic concentration range, further experiments on purified FcCAR@Ag NCs should be performed in future investigations to define safety and antibacterial selectivity data.

Conclusions

This work describes the synthesis, physicochemical properties, electrochemical behavior, and strong antimicrobial efficacy of silver nanoclusters capped with the amphiphilic dipeptide ferrocene-β-Ala-His (FcCAR). The synthetic one-step procedure involved the reduction of silver ions by an excess of ligand under basic conditions, in the presence of ascorbic acid, and with a fine-tuning of the experimental conditions, including temperature, time, and ligand/metal ions molar ratio. This eco-friendly procedure does not require the addition of an external reducing agent, and the presence of amphiphilic functional groups on the ligand plays a key role in both the formation and stabilization of silver nanoclusters. Specifically, the ferrocene unit promotes nanocluster formation; no silver nanoclusters with measurable photoluminescence were obtained when unfunctionalized carnosine was used, even in the presence of ascorbic acid. Moreover, the histidine functional groups and the ferrocene units act as stabilizing agents. The analytical, spectroscopic, and morphological results proved the successful synthetic procedure, offering information regarding the size, morphology, and colloidal stability. The intrinsic photoluminescence properties of FcCAR@Ag NCs were assessed through comprehensive spectroscopic characterization that included UV/vis and excitation/emission spectra and the determination of the absolute quantum yield (QY%). As expected, no significative surface plasmon resonance band in the 400–450 nm range of the UV/vis spectrum was observed, whereas FcCAR@Ag NCs showed high fluorescence emission at 425 nm by excitation at 390 nm.

The 5.9% QY of the blue-emitting nanoclusters is relatively high for ligand-stabilized silver nanoclusters in aqueous media, indicating that FcCAR is effective not only as a stabilizing agent but also as a photophysically active scaffold that enhances emission through its amphiphilic nature and electron-donating ferrocene moiety. Morphological analyses confirmed the nature of nanoclusters and indicated the presence of very small FcCAR@Ag NCs with a spherical-shaped morphology and a narrow particle size distribution (2.75 ± 0.35 nm).

The electrochemical behavior of FcCAR@Ag NCs investigated on screen-printed electrodes (SPEs) using cyclic voltammetry showed a reversible redox process on both SPEs and a peak anodic current almost double that of native FcCAR on screen-printed carbon electrodes (SPCEs). The enhanced electrochemical response relative to the anodic signal was also evident in differential pulse voltammetry.

The MIC and MBC values demonstrated that FcCAR@Ag NCs exhibit superior antimicrobial activity compared to the counterpart silver ions: a twofold reduction in MIC and a fourfold reduction in MBC for both *S. aureus* and *E. coli* were observed. In addition, low MIC values (5.8 μg mL^{-1}) were also found against clinically relevant bacteria, pathogens, including methicillin-resistant *S. aureus* (MRSA), vancomycin-resistant *E. faecium* (VREfm), *P. aeruginosa*, and *E. coli* (DSM 105388). Finally, FcCAR@Ag NCs were also effective in reducing 24 h established biofilms formed by *S. aureus*, *E. coli*, and *P. aeruginosa*, showing a comparable impact on total biomass and metabolic activity in *S. aureus*, while preferentially compromising biofilm biomass in *E. coli* and *P. aeruginosa*. Overall, these findings can contribute to the advancement of nanocluster chemistry and could support the ongoing efforts to translate silver nanoclusters from laboratory research to practical applications.

Author contributions

Conceptualization, investigation, and writing – original draft: Anna Piperno, Alexandru-Milentie Hada, Antonia Nostro, Angela Scala, Antonino Mazzaglia; investigation, and methodology: Markus Zetes, Marco Abbate, Nina Burduja, Ana Laura Coria-Gutiérrez, Chiara Abate; methodology, investigation, data curation: Francisco J. Terán, Ana-Maria Craciun, Milica Todea; project administration, resources, supervision: Anna Piperno. All authors have read and agreed to the published version of the manuscript.

Conflicts of interest

There are no conflicts to declare.

Abbreviations

AA	Ascorbic acid
Ag NCs	Silver nanoclusters
AgÅPs	Ultrasmall silver particles
$AgNO_3$	Silver nitrate
ANOVA	Two-way analysis of variance
CLSI	Clinical and Laboratory Standards Institute
CV	Cyclic voltammetry
D_H	Hydrodynamic diameter
DLS	Dynamic light scattering
DPV	Differential pulse voltammetry
ESBLs	Extended-spectrum β-lactamases
FcCAR	Ferrocenyl carboxylic acid
MBC	Minimum bactericidal concentration
MDR	Multidrug-resistant
MIC	Minimum inhibitory concentration
MRSA	Methicillin-resistant *Staphylococcus aureus*
MHB	Mueller–Hinton broth
NaOH	Sodium hydroxide
NCs	Metal nanoclusters
PCS	Photon correlation spectroscopy
PL	Photoluminescence
pAg NCs	Polycationic silver nanoclusters
QY	Quantum yield
RE	Reference electrode
SD	Standard deviation
SPCEs	Screen-printed carbon electrodes
SPEs	Screen-printed electrodes
Pt-SPEs	Screen-printed platinum electrodes
TEM	Transmission electron microscopy
TGA	Thermogravimetric analysis
TSD	Tryptic soy broth
VREfm	Vancomycin-resistant *Enterococcus faecium*
ζ	Zeta potential

Data availability

The data supporting this article have been included as part of the supplementary information (SI). Supplementary information: TGA of FcCAR@AgNCs, brownish FcCAR@Ag NCs solution under ambient light and under UV irradiation, fluorescence excitation spectra of FcCAR@Ag NCs (λ_{em} = 425 nm), UV/vis absorption and excitation/emission spectra of stored samples, high-resolution XPS analysis, electroactive surface area, MIC values of clinically relevant antibiotics, and cell viability analysis. See DOI: https://doi.org/10.1039/d6tb00577b.

Acknowledgements

This work was partially supported by MUR PON Italy ''Ricerca e Innovazione'' 2014–2020 Azione IV ''Dottorati e Contratti di ricerca su tematiche dell'Innovazione''; by STRIKE-Comprehensive strategies to tackle malignant tumors: from nanomedicine and theranostics to precision medicine (HORIZON-MSCA-2021-DN-01 No. 101072462), by the European Union (NextGeneration EU) through the MUR-PNRR project SAMOTHRACE (ECS00000022), and by the Comunidad de Madrid through project TEC-2024/TEC-380 (Mag4TIC-CM)

References

1 P. Mahato, S. Shekhar, S. Agrawal, S. Pramanik and S. Mukherjee, *ACS Appl. Nano Mater.*, 2022, **5**, 7571–7579.
2 J. Y. Oh, K. E. Villaseñor, A. C. Kian and D. P. Cormode, *ACS Appl. Mater. Interfaces*, 2025, **17**, 28982–29001.
3 H. Yin, M. Zhou, X. Chen, T. F. Wan, L. Jin, S. S. Rao, Y. J. Tan, R. Duan, Y. Zhang, Z. X. Wang, Y. Y. Wang, Z. H. He, M. J. Luo, X. K. Hu, Y. Wang, W. Y. Situ, S. Y. Tang, W. E. Liu, C. Y. Chen and H. Xie, *Theranostics*, 2021, **11**, 8152–8171.
4 L. Chen, A. Black, W. J. Parak, C. Klinke and I. Chakraborty, *Aggregate*, 2022, **3**, 1–18.
5 A. M. Hada, M. Zetes, M. Focsan, S. Astilean and A. M. Craciun, *Int. J. Mol. Sci.*, 2022, **23**(20), 12410.
6 P. Maity, P. De, S. Ghosh, V. Jha, S. De, S. P. Senanayak and D. Samanta, *Chem. Mater.*, 2026, **38**(4), 2004–2016.
7 R. E. Ruther, Q. Cui and R. J. Hamers, *J. Am. Chem. Soc.*, 2013, **135**, 5751–5761.
8 Z. Guo, Y. Chen, Y. Wang, H. Jiang and X. Wang, *J. Mater. Chem. B*, 2020, **8**, 4764–4777.
9 A. M. Hada, M. Lamy de la Chapelle, M. Focsan and S. Astilean, *Molecules*, 2025, **30**, 1–39.
10 J. Meng, Z. Hu, M. He, J. Wang and X. Chen, *J. Colloid Interface Sci.*, 2021, **602**, 846–858.
11 Y. Shi, Z. Liang, M. Jiang, J. Qin, X. Fei, Y. Chen, X. Yu, K. Pu and X. Ma, *Chem. Mater.*, 2024, **36**(18), 8673–8681.
12 R. Bélteki, L. Kuklis, G. Gombár, D. Ungor and E. Csapó, *Chem. – A Eur. J.*, 2023, **29**, e202300720.
13 J. Xu, M. Ramasamy, T. Tang, Y. Wang, W. Zhao and K. C. Tam, *J. Colloid Interface Sci.*, 2022, **623**, 883–896.
14 C. Abate, G. Neri, M. Abbate, M. Cordaro, P. G. Mineo, E. Fazio, C. Corsaro, O. Giuffré, C. Foti and A. Piperno, *RSC Adv.*, 2025, **15**, 23596–23604.
15 J. Kong, S. Zhao, X. Han, W. Li, J. Zhang, Y. Wang, X. Shen, Y. Xia and Z. Li, *Anal. Chem.*, 2023, **95**, 5053–5060.
16 C. Abate, G. Neri, A. Scala, P. G. Mineo, E. Fazio, A. Mazzaglia, A. Fragoso, O. Giuffrè, C. Foti and A. Piperno, *ACS Appl. Nano Mater.*, 2023, **6**, 17187–17195.
17 Y. Chen, L. Ren, L. Sun, X. Bai, G. Zhuang, B. Cao, G. Hu, N. Zheng and S. Liu, *NPG Asia Mater.*, 2020, **12**, 56.
18 H. Haidari, R. Bright, Z. Kopecki, P. S. Zilm, S. Garg, A. J. Cowin, K. Vasilev and N. Goswami, *ACS Appl. Mater. Interfaces*, 2022, **14**, 390–403.
19 J. Yang, F. Yang, C. Zhang, X. He and R. Jin, *ACS Mater. Lett.*, 2022, **4**, 1279–1296.
20 Y. Y. Li, K. Xia, Y. W. Liu, Y. J. Tan, H. M. Li, Y. Y. Wang, S. K. Feng, L. Jin, T. F. Wan, J. Cao, C. Y. Chen, Z. Z. Liu, X. K. Hu, B. Wu, Y. Wang, Z. H. He, H. Yin, W. Y. Situ, L. Y. Qi, Z. X. Wang and H. Xie, *Adv. Ther.*, 2023, **6**, 1–12.

21 A. G. Vivancos, Y. Zhou, U. Lappan, S. Boye, L. Muñoz-Moreno, D. Appelhans and S. Moreno, *J. Mater. Chem. B*, 2025, **13**, 1980–1990.
22 J. Li, S. Yan, J. Xu, C. Li and Q. Yu, *J. Mater. Chem. B*, 2025, **13**, 11166–11200.
23 J. E. Kellon, S. L. Young and J. E. Hutchison, *Chem. Mater.*, 2019, **31**, 2685–2701.
24 J. Li, Y. Feng, W. Chen, S. Zhang, J. Ma, S. Chen, S. Liu, C. Cao and Y. Zhang, *Prog. Mater. Sci.*, 2023, **132**, 101045.
25 M. Jiang, M. Wang, W. Lai, H. Ren, H. Li, Y. Qi, C. Hong and S. Chen, *Anal. Chem.*, 2025, **97**, 22380–22389.
26 C. Abate, A. Piperno, A. Fragoso, O. Giuffrè, A. Mazzaglia, A. Scala and C. Foti, *Dalton Trans.*, 2023, **52**, 3699–3708.
27 M. Ip, S. L. Lui, V. K. M. Poon, I. Lung and A. Burd, *J. Med. Microbiol.*, 2006, **55**, 59–63.
28 M. P. Weinstein, B. Limbago, J. Patel, B. A. J. Mathers, C.-A. Burnham, T. Mazzulli, S. Campeau, S. D. Munro, P. S. Conville, M. Ordoñez Smith de Danies, C. Doern, R. Patel, G. M. Eliopoulos, S. S. Richter, M. F. Galas, M. Satlin, R. M. Humphries, J. M. Swenson, S. G. Jenkins, A. Wong, S. M. Kircher, W. F. Wang, J. S. Lewis II and B. L. Zimmer, *Methods for Dilution Antimicrobial Susceptibility Tests for Bacteria That Grow Aerobically; Approved Standard*, Clinical and Laboratory Standards Institute, Wayne, PA, 11th edn, 2018.
29 E. Marini, M. Di Giulio, G. Ginestra, G. Magi, S. Di Lodovico, A. Marino, B. Facinelli, L. Cellini and A. Nostro, *PLoS One*, 2019, **14**, 1–12.
30 A. M. Hada, A. M. Craciun, M. Focsan, R. Borlan, O. Soritau, M. Todea and S. Astilean, *Talanta*, 2021, **225**, 121960.
31 Y. Zhang, D. Sun, J. Shen and X. Xin, *Appl. Surf. Sci.*, 2020, **514**, 145913.
32 M. Huang, J. Kong, J. Zhang, Z. Wang, D. Hao, J. Zhang, Y. Wang, W. Qi, R. Su and Z. He, *Part. Part. Syst. Charact.*, 2022, **39**, 1–9.
33 H. Haidari, R. Bright, Z. Kopecki, P. S. Zilm, S. Garg, A. J. Cowin, K. Vasilev and N. Goswami, *ACS Appl. Mater. Interfaces*, 2022, **14**, 390–403.
34 H. Yamada, K. Yoshii, M. Asahi, M. Chiku and Y. Kitazumi, *Electrochemistry*, 2022, **90**, 1–8.
35 N. Aristov and A. Habekost, *World J. Chem. Educ.*, 2015, **3**, 115–119.
36 S. Fulaz, H. Devlin, S. Vitale, L. Quinn, J. P. O. Gara and E. Casey, *Int. J. Nanomed.*, 2020, **15**, 4779–4791.
37 R. M. Pinto, D. Lopes-de-campos, M. C. L. Martins, S. Reis and P. Van Dijck, *FEMS Microbiol. Rev.*, 2019, **43**, 622–641.
38 T. Wang, Y. Li, Y. Liu, Z. Xu, M. Wen, L. Zhang, Y. Xue and L. Shang, *J. Colloid Interface Sci.*, 2023, **633**, 851–865.
39 H. Tan, H. Zhou, Y. Zhao, X. Wang, X. He, J. Chen, K. Zhang, R. Antoine, S. Zhang and Y. Tian, *J. Phys. Chem. C*, 2022, **126**, 5198–5205.